Regular Article

PHYSICAL CHEMISTRY RESEARCH
Published by the
Iranian Chemical Society
www.physchemres.org
info@physchemres.org

Phys. Chem. Res., Vol. 11, No. 1, 33-48, March 2023
DOI: 10.22036/pcr.2022.330752.2035

Molecular Structure, Linear, and Nonlinear Optical Properties of Piperazine-1,4-Diium Bis 2,4,6-Trinitrophenolate: A Theoretical Investigation

F. Yahia Cherif[a,b], D. Hadji[a,b,*] and N. Benhalima[c]

[a]*Laboratoire de Modélisation et de Méthodes de Calcul, Université de Saïda-Dr. Moulay Tahar, Algérie*
[b]*Département de Chimie, Faculté des Sciences, Université de Saïda-Dr. Moulay Tahar, Algérie*
[c]*Laboratory of Technology and Solid Properties (LTPS), Abdelhamid Ibn Badis University of Mostaganem, 27000 Mostaganem, Algeria*
(Received 21 February 2022, Accepted 27 April 2022)

In this study, the molecular structure, vibrational spectra, and linear and nonlinear optical properties of piperazine-1,4-diium bis 2,4,6-trinitrophenolate were theoretically investigated using density functional theory at several levels. To examine the linear and nonlinear optical behavior of the studied compound, dipole moment, polarizability, and first order hyperpolarizability (β) were calculated and analysed in detail. The hyper-Rayleigh scattering first hyperpolarizability, electric-field-induced second harmonic generation, and depolarization ratios were the targeted quantities. The NO_2, NH_2, C=C, C-N groups and phenolic O atom were identified using theoretical vibrational analysis. The highest occupied molecular orbital, lowest unoccupied molecular orbital, and their energy gap were also calculated. Furthermore, global chemical reactivity descriptors and the three-dimensional molecular electrostatic potential were studied and discussed. The results of the calculations highlighted the following: 1) Predicted geometrical parameters highly correlated with the corresponding experimental ones; 2) A good correlation was observed between the calculated and experimental vibration frequencies; 3) A direct relationship was observed between the energy gap and β has been obtained; 4) The calculated variation in β confirmed the nonlinear optical activity of the studied piperazine. This study can help deepen our understanding of the nonlinear optical properties of piperazine-based molecules and provide guidance on the rational design of molecules with excellent optoelectronic properties.

Keywords: Piperazine, Molecular structure, Hydrogen bond, Hyperpolarizability

INTRODUCTION

The development of photonic technology during the past decade has intensified research on the search for new materials that display unusual and interesting nonlinear optical (NLO) properties. The search for new materials with high optical nonlinearities has been considered an important endeavour due to the application of such materials in harmonic generation, amplitude and phase modulation, and other signal processing tools [1-5]. Second-order NLO crystals are widely used to convert the frequency of coherent laser sources. Compared to different types of NLO materials, organic materials are more suitable due to their high electronic susceptibility, facile modification through standard synthetic methods, and relative ease of processing [6]. Organic complexes are used in different pharmaceutical applications [7,8], microemulsion systems, and organic semiconductors [9,10]. In general, π-electron conjugation systems in organic molecules are asymmetrised by the electron donor and acceptor groups, which are easily polarizable. The strong charge-transfer (CT) between such groups operating across the entire extended system can markedly increase the optical nonlinearity of their structure. Additionally, the formation of hydrogen bonds in molecular packing has been recognized as a key factor in self-assembly or molecular recognition processes when

*Corresponding author. E-mail: djebar.hadji@univ-saida.dz

extensive structures are formed from crystal building blocks or supramolecular synthons [11]. The study of NLO properties of organic compounds such as piperazine has been viewed as the most important building block of recent drug discoveries [12,13]. Piperazine is an organic amine compound that consists of a six-membered ring containing two nitrogen atoms at opposite positions. The non-aromatic six-membered heterocycle adopts a chair conformation. Piperazines and substituted piperazines are important pharmacophores that can be found in many biologically active compounds across a number of different therapeutic areas, such as antifungal [14], antibacterial, antimalarial, and antipsychotic agents [15]. A valuable insight into recent advances in antimicrobial activity of piperazine derivatives has been reported [16]. Also, a picric acid can be used to form salts with electrostatic forces and multiple hydrogen bonds, which are known to improve the quality of crystalline materials. Picric acid derivatives are used in human therapy, such as the treatment of burns and antiseptic and astringent agents [17]. Moreover, several complexes of picric acid with organic basic molecules can be used in pharmaceutical and nonlinear applications [18]. Donor-acceptor groups in benzene derivatives produce high molecular nonlinearity. The adducts of picric acid and piperazine have been reported to possess a supramolecular structure [19]. There is an increasing demand for the use and application of single crystals in the development of technology and devices due to their NLO property. Some related compounds, *viz*., 1-[4-(4-hydroxyphenyl)piperazin-1-yl]ethanone [20], 3-(Z)-isobutylidene-1-acetylpiperazine-2,5-dione [21], piperazine-1,4-diium picrate-piperazine [19], cinnarizinium picrate [22], 1-piperonylpiperazinium picrate [23], and piperazine-1,4-diium bis 2,4,6-trinitrophenolate (PDBT) [24], have been reported to have crystal structures. In view of the importance of PDBT, this paper aimed to conduct a comparative study between the experimental and the theoretical properties of this compound. PDBT was synthesized and crystallized using piperazine and picric acid, as starting materials, by the slow evaporation method [24]. The growth of the crystal of PDBT was followed by detailed characterization studies of single-crystal X-ray diffraction (XRD) and infrared (IR) spectroscopy. The optical properties of the crystal were studied by ultraviolet-visible (UV-Vis) near IR spectroscopy to explore its optical transmission. The second-harmonic generation (SHG) of the crystal was tested to confirm the NLO properties [24]. The theoretical properties were calculated using density functional theory (DFT). The optimized geometry of PDBT was evaluated by applying DFT. Molecular structural parameters, vibrational spectra, and vibrational assignments were determined based on the potential energy distribution (PED). The UV-Vis spectroscopic studies, together with the highest occupied molecular orbital (HOMO) and lowest unoccupied molecular orbital (LUMO), were used to obtain information regarding the CT within the molecule. In addition, detailed linear and NLO properties were calculated by computing and analysing dipole moment (μ), polarizability (α), and first-order hyperpolarizability (β). The three-dimensional molecular electrostatic potential (MESP) and global chemical reactivity descriptors (GCRD) were also calculated to investigate the reactive nature of PDBT.

COMPUTATIONAL DETAILS

The geometric structure of the studied piperazine was fully optimized using DFT with the B3LYP functional and without any constraint in the gas phase [25]. Figure 1 and Table S1 (see the Supporting Information (SI)) show the optimized molecular geometry and its coordinates, respectively. Pople basis set 6-311+G(d,p) was employed for all atoms [26-28]. The calculation was converged to an optimized geometry corresponding to the lowest energy. Positive vibrational frequencies confirmed the stability of the optimized geometry. The final geometry was used to predict the geometric parameters and compared with those of the XRD data [24]. The theoretical vibrational spectra of the title compound and their detailed assignments were calculated at the same level of theory of the respective optimization process and interpreted based on PED analysis using the VEDA 4 program [29]. The μ, α, and β were calculated using the MP2 [30], B3LYP, PBE0 [31], CAM-B3LYP [32], ωB97X-D [33], and M06-2X [34] DFT functionals. The total $\mu$are was defined as follows:

$$\mu = \sqrt{(\mu_x^2 + \mu_y^2 + \mu_z^2)} \quad (1)$$

The two following properties were calculated for α: the

mean polarizability (Δα) and the polarizability anisotropy <α>. α was calculated from α components as follows:

$$< \alpha > \frac{1}{3} \sum_{i=x,y,z} \alpha_{ii} \quad (2)$$

$$< \alpha > = \frac{1}{3}(\alpha_{xx} + \alpha_{yy} + \alpha_{zz}) \quad (3)$$

and the Δα was calculated as shown below:

$$\Delta\alpha = \sqrt{\frac{1}{2}\left((\alpha_{xx} - \alpha_{yy})^2 + (\alpha_{xx} - \alpha_{zz})^2 + (\alpha_{yy} - \alpha_{zz})^2\right)} \quad (4)$$

To obtain β, the total first hyperpolarizability β_{tot}, the hyper-Rayleigh scattering (HRS) first hyperpolarizability β_{HRS} (-2ω; ω, ω), the electric field-induced second-harmonic generation (EFISHG) $\beta_{//}$ (-2ω; ω, ω), and depolarization ratios (DR) were calculated. All calculations were performed using Gaussian 09 [35]. The visualization of the structure and density plots of HOMO and LUMO was carried out using GaussView 5.01 [36]. The scattering intensity corresponding to the polarization angle (Ψ) was obtained by the Multiwfn 3.7(dev) code [37,38]. The central quantity in EFISHG was $\beta_{//}$, and the vector component of β was projected along the μ axis (multiplied by 3/5).

,

$$\beta_{//}(-2\omega;\omega,\omega) = \beta_{//} = \frac{1}{S}\sum_i \frac{\mu_i}{|\vec{\mu}|}\sum_j (\beta_{ijj} + \beta_{jij} + \beta_{jji}) = \frac{3}{5}\sum_i \frac{\mu_i \beta_i}{|\vec{\mu}|} \quad (5)$$

where $|\vec{\mu}|$ is the norm of the dipole moment, μ_i is the components of the μ vectors, and β_i is the i^{th} components of the β vectors. The β_{HRS} property is related to the HRS intensity for non-polarized incident light and the observation of plane-polarized scattered light made perpendicularly to the propagation plane. The full β_{HRS} reads as follows:

,

$$\beta_{HRS}(-2\omega;\omega,\omega) = \sqrt{\{< \beta^2_{ZZZ} > + < \beta^2_{ZXX} >\}} \quad (6)$$

and the DR is presented below:

$$DR = \frac{I^{2\omega}_{VV}}{I^{2\omega}_{HV}} = \frac{< \beta^2_{ZZZ} >}{< \beta^2_{ZXX} >} \quad (7)$$

These HRS invariants $< \beta^2_{ZZz} >$ and $< \beta^2_{ZXx} >$ are orientational averages of the β tensor and were calculated without assuming Kleinman's conditions. $< \beta^2_{ZZz} >$ and $< \beta^2_{ZXx} >$ were defined as follows:

$$< \beta^2_{ZZz} > = \frac{1}{7}\sum_{\varsigma}^{x,y,z}\beta^2_{\varsigma\varsigma\varsigma} + \frac{4}{35}\sum_{\varsigma\neq\eta}^{x,y,z}\beta^2_{\varsigma\varsigma\eta} + \frac{2}{35}\sum_{\varsigma\neq\eta}^{x,y,z}\beta_{\varsigma\varsigma\varsigma}\beta_{\varsigma\eta\eta} + \frac{4}{35}\sum_{\varsigma\neq\eta}^{x,y,z}\beta_{\eta\varsigma\varsigma}\beta_{\varsigma\varsigma\eta} + \frac{4}{35}\sum_{\varsigma\neq\eta}^{x,y,z}\beta_{\varsigma\varsigma\varsigma}\beta_{\eta\eta\varsigma} + \frac{1}{35}\sum_{\varsigma\neq\eta}^{x,y,z}\beta^2_{\eta\varsigma\varsigma} + \frac{4}{105}\sum_{\varsigma\neq\eta\neq\varepsilon}^{x,y,z}\beta_{\varsigma\varsigma\eta}\beta_{\eta\varepsilon\varepsilon} + \frac{1}{105}\sum_{\varsigma\neq\eta\neq\varepsilon}^{x,y,z}\beta_{\eta\varsigma\varsigma}\beta_{\eta\varepsilon\varepsilon} + \frac{4}{105}\sum_{\varsigma\neq\eta\neq\varepsilon}^{x,y,z}\beta_{\varsigma\varsigma\eta}\beta_{\varepsilon\varepsilon\eta} + \frac{2}{105}\sum_{\varsigma\neq\eta\neq\varepsilon}^{x,y,z}\beta^2_{\varsigma\eta\varepsilon} + \frac{4}{105}\sum_{\varsigma\neq\eta\neq\varepsilon}^{x,y,z}\beta_{\varsigma\eta\varepsilon}\beta_{\eta\varsigma\varepsilon} \quad (8)$$

$$< \beta^2_{ZZz} > = \frac{1}{35}\sum_{\varsigma}^{x,y,z}\beta^2_{\varsigma\varsigma\varsigma} + \frac{4}{105}\sum_{\varsigma\neq\eta}^{x,y,z}\beta_{\varsigma\varsigma\varsigma}\beta_{\varsigma\eta\eta} - \frac{2}{35}\sum_{\varsigma\neq\eta}^{x,y,z}\beta_{\varsigma\varsigma\varsigma}\beta_{\eta\eta\varsigma} + \frac{8}{105}\sum_{\varsigma\neq\eta}^{x,y,z}\beta^2_{\varsigma\varsigma\eta} + \frac{3}{35}\sum_{\varsigma\neq\eta}^{x,y,z}\beta^2_{\varsigma\eta\eta} - \frac{2}{35}\sum_{\varsigma\neq\eta}^{x,y,z}\beta_{\varsigma\varsigma\eta}\beta_{\eta\varsigma\varsigma} + \frac{1}{35}\sum_{\varsigma\neq\eta}^{x,y,z}\beta_{\varsigma\eta\eta}\beta_{\varsigma\varepsilon\varepsilon} - \frac{2}{105}\sum_{\varsigma\neq\eta\neq\varepsilon}^{x,y,z}\beta_{\varsigma\varsigma\eta}\beta_{\eta\varepsilon\varepsilon} + \frac{2}{35}\sum_{\varsigma\neq\eta\neq\varepsilon}^{x,y,z}\beta^2_{\varsigma\eta\varepsilon} - \frac{2}{105}\sum_{\varsigma\neq\eta\neq\varepsilon}^{x,y,z}\beta_{\varsigma\eta\varepsilon}\beta_{\eta\varsigma\varepsilon} \quad (9)$$

The full formula and more calculation details are provided in SI and can be found in Ref. [39].

The GCRD, such as electronegativity (χ), chemical hardness (η), chemical softness (S), and electrophilicity index (ω), were deduced from HOMO-LUMO analysis employing B3LYP, PBE0, CAM-B3LYP, ωB97X-D, and M06-2X functionals with 6-311+G(d,p) basis set. The MESP at the B3LYP/6-311+G(d,p) level was calculated to predict reactive sites of electrophilic or nucleophilic attacks on the investigated molecule.

RESULTS AND DISCUSSION

Ground State Geometry

The optimized structure of PDBT at the B3LYP/6-311+G(d,p) level of theory with atomic labelling is shown in Fig. 1. The agreement between the experimental crystal structure [24] and the optimized geometry was excellent, showing that the B3LYP/6-311+G(d,p) level reproduced the experimental structure of the studied piperazine. Several studies [40-41] have shown the ability of the B3LYP level to describe the geometry of conjugated systems.

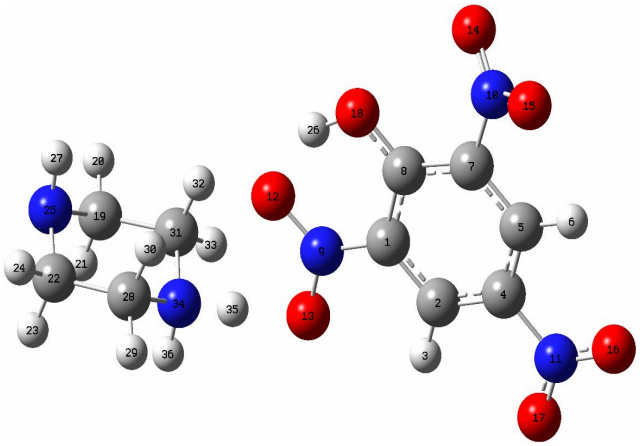

Fig. 1. PDBT optimized geometry at the B3LYP/6-311+G(d,p) level.

The selected geometrical parameters (*i.e.*, bond lengths, bond angles, and torsion angles) are summarized in Table 1. The calculated parameters using the B3LYP functional were in agreement with the XRD data [24].

Table 1. Bond Lengths, Bond Angles, and Torsion Angles Calculated Using the B3LYP/6-311+G(d,p) Level

Bond length	XRD[a]	B3LYP/6-311+G(d,p)
C1–C2	1.3692	1.398
C1–C8	1.439	1.435
C1–N9	1.4576	1.394
C2–C4	1.382	1.389
C2–H3	0.93	1.079
C4–C5	1.377	1.387
C4–N11	1.4457	1.471
C5–C7	1.367	1.390
C7–C8	1.4369	1.405
C7–N10	1.4555	1.474
C8–O18	1.2580	1.324
C19–N25	1.483	1.460
C19–C31	1.509	1.530
C19–H21	0.97	1.098
C19–H20	0.97	1.092
C19–N25	1.4808	1.460
N9–O13	1.2148	1.302
N9–O12	1.2198	1.311
N10–O14	1.2191	1.220
N10–O15	1.2193	1.227
N11–O17	1.2158	1.227
N11–O16	1.2273	1.226
N34–H35	0.892	1.089
N34–H36	0.865	1.021
Bond angle		
C7–C5–C4	118.8	118.2
C7–C5–H6	120.6	120.5
C5–C7–C8	124.6	122.9
C5–C7–N10	116.4	116.9
C8–C7–N10	119.0	120.3
O18–C8–C7	123.6	121.0
O18–C8–C1	124.4	122.1
C7–C8–C1	112.0	116.9
N25–C19–C31	110.8	113.5
N25–C19–H21	109.5	108.0
C2–C1–N9	116.3	119.2
C8–C1–N9	119.5	120.2
C1–C2–C4	119.0	119.3
C1–C2–H3	120.5	119.6
C5–C4–C2	121.3	121.9
C5–C4–N11	119.4	122.1
H32–C31–H33	108.1	108.3
O13–N9–O12	122.8	119.1
O13–N9–C1	118.0	119.5
O12–N9–C1	119.2	121.4
O14–N10–C7	119.4	118.1
O15–N10–C7	117.2	116.7
O17–N11–O16	123.2	124.6
O17–N11–C4	118.8	117.7
O16–N11–C4	118.1	117.7
C31–N19–C25	112.2	113.9
C31–N34–H36	110.0	109.8
C19–N25–H27	108.7	111.1
Dihedral angle		
C8–C1–C2–C4		
C1–C2–C4–N11	176.1	179.8
C5–C7–C8–O18	177.8	177.3
N10–C7–C8–O18	0.4	–2.6
C28–C22–N25–C19	55.9	52.3
N9–C1–C8–C7	178.5	179.3
C8–C7–N10–O15	156.7	143.1
C2–C1–N9–O12	155.0	179.5
C5–C7–N10–O14	147.9	141.6
C8–C7–N10–O15	146.8	143.1
C2–C4–N11–O17	3.1	–0.5
C5–C4–N11–O16	1.5	–0.6

Note: Comparisons were made with the experimental data digitized from Ref. [24]; [a] = XR measurement [24].

The theoretical and experimental data [24] showed that the C–C bond lengths were in the range of 1.367 to 1.522 Å. It was also observed that in the benzene ring, the C–C bond lengths had an average value of 1.38 and 1.53 Å obtained by XRD measurements [24] and the B3LYP/6–311+G(d,p) level, respectively. The calculated C6–O7 bond length at the B3LYP/6-311+G(d,p) level (1.324 Å) was notably shorter than the normal C–O single bond (1.427 Å) [42] due to the conjugation. The shortened C1–C2 (1.398 Å) and C4–C5 bonds (1.387 Å) can be justified by the repulsive interactions between the deprotonated O7 and the withdrawing NO_2 groups attached to the ortho positions by O7. In the picric group, the calculated C–N bond lengths varied in the range of 1.394 to 1.471 Å. However, the value of the C–N bond lengths in the piperazine ring was approximately 1.46 Å. In the NO_2, the experimental N–O bond length value was 1.219 Å, which was slightly lower than the corresponding calculated value (1.23 Å) due to the presence of intermolecular interactions involving oxygen atoms. It must be noted that the position of hydrogens cannot generally be determined accurately *via* XRD and this is why the experimental bond lengths and dihedrals involving hydrogen atoms differed significantly from the calculated ones. Concerning N–H bond lengths in the piperazine ring, the experimental bond lengths were shorter than the calculated ones. Figure 2 shows the shortening of the N–H bond and the closeness of oxygen to hydrogen, thus forming the N34–H35…O13 hydrogen bond. The hydrogen bonding interactions are given in Table 2. The N–H…O hydrogen bonding interaction enhanced the molecular stability of the compound. Good agreement was obtained between the experiment and the calculated bond angles. The C5–C7–N10 and C8–C7–N10 experimental bond angles were found to be 116.4° and 119.0°, respectively, and their calculated angles were found to be 115.7° and 121.2°, respectively. The difference between the experimental and calculated values of bond lengths did not exceed 2.5°. According to the above results, the dihedral angles differed by not more than 3.5°, except for the N9–C1–C8–C7 and C8–C7–N10–O15 angles, for which the dihedral angles differed by 3.91° and 26.85°, respectively. The experimental O14–N10–C7–C8 and O12–N9–C1–C8 torsion angles were found to be 34.5° and 25.1º, respectively [24]. These angles were calculated at -28.17° and -6.16°, respectively. Based on the data related to these torsion angles, it was found that NO_2 groups in the ortho position were generally involved in hydrogen bond interactions.

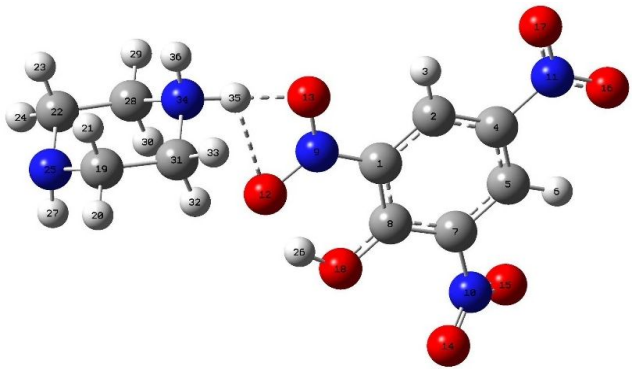

Fig. 2. Hydrogen bonds for the optimized geometry of PDBT at the B3LYP/6–311+G(d,p) level.

IR Spectroscopic Characterization

IR spectroscopy has been widely used as a reliable tool for identifying vibrational modes and functional groups in organic compounds. The vibrational frequencies were

Table 2. A Comparison of the Theoretical and Experimental Hydrogen Bonds (Å, °) of PDBT

		D–H	H…A	D...A	D–H…A
N34-H(35)...O(13)	RX[a]	0.892	1.987	2.7872	148.5
	B3LYP	1.089	1.534	2.6225	178.9
N34-H(35)...O(12)	RX[a]	0.892	2.419	3.0823	131.3
	B3LYP	1.089	2.437	3.0529	114.5

Note: [a] = XR measurements [24].

calculated using the B3LYP/6-311+G(d,p) level. PDBT consists of 36 atoms; these atoms have 102 (3N–6) normal modes of vibrations, from 4000 to 0 cm^{-1}, of which the strongest and weakest absorption modes are observed at 2332.76 cm^{-1} and 525.23 cm^{-1}, respectively. The PED was calculated for each normal mode. Contributions lower than 10% were not considered. The observed IR modes with their relative intensities and computed vibrational frequencies and the assignments of PDBT are presented in Table S2. Due to the overestimation of the experimental values obtained through the DFT calculations, the calculated wavenumbers were scaled using the recommended set of transferable scale factors [43]. Therefore, the main modes of vibration were estimated by scale factors as follows: ~0.953 for ν(C–H_{Ph}), 0.943 for ν(N–H_{Pi}), 0.98 for ν(C–$H2_{asPi}$), 0.95 for ν(C–$H2_{sPi}$), 0.925 for ν(NO_{2as}), 0.975 for ν(NO_{2s}), and ~0.98 for ν(O–H) [43-46]. The experimental IR spectrum of PDBT, recorded in the spectral range of 4000-400 cm^{-1}, and the calculated IR spectrum obtained using the B3LYP/6-311+G(d,p) level are shown in Fig. 3. As can be seen in Fig. 3 and Table S2, the vibration mode 89 was related to the N–H stretching vibration of piperazine. This vibration was observed at 3318 cm^{-1}. The ν(NH) vibration wavenumbers were calculated using the B3LYP/6-311+G(d,p) level, and its corresponding value was 3471.15 cm^{-1}. NO_2 stretching vibrations were the most characteristic bands in the IR spectra of aromatic compounds with NO_2 moiety in their structures. These vibrations varied between symmetric $\nu_s(NO_2)$ and asymmetric $\nu_{as}(NO_2)$ stretching vibrations with strong absorption intensities. In addition, $\nu_{as}(NO_2)$ and $\nu_s(NO_2)$ stretching vibrations appeared in the range of 1570-1485 and 1370-1320 cm^{-1}, respectively [47]. In our study, $\nu_{as}(NO_2)$ and $\nu_s(NO_2)$ stretching vibrations were found to be at 1467 cm^{-1} (PED 61%) and 1322 cm^{-1} (PED 73%), respectively. The corresponding experimental stretching vibration values appeared at 1436 cm^{-1} for $\nu_{as}(NO_2)$ and 1321 cm^{-1} for $\nu_s(NO_2)$. The C–H stretching vibrations in aromatic compounds varied between 3100 and 3000 cm^{-1} [48]. As detailed in Table S2, these vibrations were calculated in the range of 3262.65-3249.65 cm^{-1} using the B3LYP/6-311+G(d,p) level. The bands corresponding to CH_2 stretching vibrations were observed between 3000 and 2865 cm^{-1} [49]. The experimental asymmetric and symmetric stretching vibrations were identified at 3068 and 2841 cm^{-1}, respectively. The corresponding theoretical asymmetric and symmetric stretching vibrations were in the range of 3072-3034 cm^{-1} and 2922-2861 cm^{-1} using the B3LYP/6-311+G(d,p) level. The N–H asymmetric and symmetric stretching vibrations of the studied piperazine were observed at 3318 cm^{-1} [24] and 3207 cm^{-1} [50], respectively. In the present study, the corresponding theoretical values were calculated at 3322 and 3273 cm^{-1}, respectively, with a PED of 100%. Furthermore, the HNH deformation band [δ(HNH)], with a PED of 66%, was computed using the B3LYP/6-311+G(d,p) level, and its value was found to be 1736 cm^{-1}. The stretching vibration of C=C was observed at 1624 cm^{-1}, and the computed value was 1632 cm^{-1}. The presence of peaks corresponding to 1273 cm^{-1} was due to the presence of phenolic O atoms (C=O stretching vibrations). The computed value was 1279 cm^{-1}, with a contribution of 43%. As can be seen in Table S2, the vibration mode 96 was related to the O–H stretching vibration ν(OH). These vibration wavenumbers were calculated using the B3LYP functional, and the corresponding scaled values were 3052 cm^{-1}, with a PED of 98%. The lower peaks at 932 cm^{-1} were due to the scissoring of NO_2. The value 108 cm^{-1} was due to torsion vibrations in the τON_{Ph}…HN, τH…NCC_{Ph}, and τCNH_{Pi}…N, which confirms the formation of the hydrogen bond.

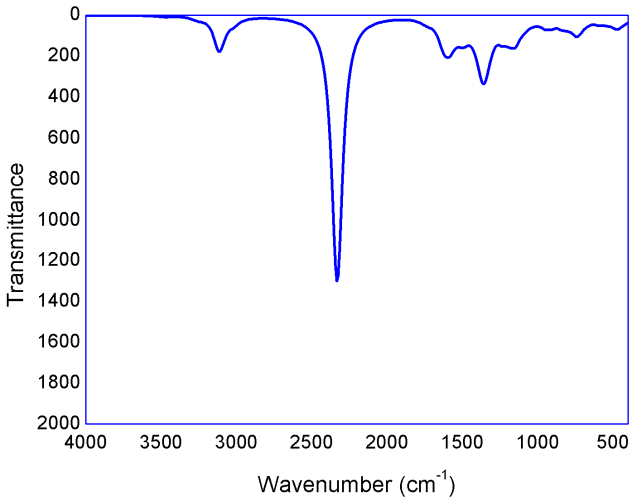

Fig. 3. The simulated IR spectrum of PDBT at the B3LYP/6-311+G(d,p) level.

Linear and NLO Properties

The accurate calculation of linear and NLO properties requires extended basis sets. It is clear that due to computational reasons, moderate size basis sets are preferable [51-52]. In this study, to find a balance between precision and calculation needs, the 6-311+G(d,p) basis set was selected. Theoretical studies of linear and NLO properties of medium size molecules have shown that the 6-311+G(d,p) basis set can give almost identical results of β to that obtained using the Dunning's correlation consistent basis set [53-55]. In the present study, high <α> values were obtained for PDBT, which ranged from 194.65 to 261.25 a.u. using the M06-2X and PBE0 functionals, respectively. The PBE0 resulted in high <α> values (371.65 a.u.) compared to other DFT functionals. Similar to what was reported in Adamo *et al.'s* [56] DFT study of polarizabilities of reference molecules H_2O, NH_3, HF, H_2S, and CO and their related theoretical study [57], in this study, it was observed that the PBE0 gave good α values among all DFT functionals. Also, in their α calculation of diphenyl ferrocenyl butentfe derivatives, Hadji *et al*. [58] confirmed α that the PBE0 results were entirely congruent with second-order Møller-Plesset perturbation theory (MP2) calculations. In this study, the MP2 method, compared to B3LYP, PBE0, ωB97X-D, and M06-2X, resulted in an <α> value somewhat closer to the PBE0 one <α>. The calculated <α> value differed by about 13% from the PBE0. For Δα, the difference between the MP2 and the PBE0 values did not exceed 20%. According to the published literature, the presence of space charge polarization provides more flexibility and can enhance the α and β of materials [59-60]. In their study of second-order NLO properties of [2.2] paracyclophane isomers, Ye *et al.* [61] showed that the space charge provided more flexibility and possibility to regulate the NLO properties of the compound. They also demonstrated that the additional typical space charge skeleton led to intramolecular donor-acceptor interactions [61]. In the PDBT studied in the present research, the presence of space charge polarization affected both α and β values. It was also observed that the PBE0/6-311+G(d,p) level, compared to other DFT levels used in this study, yielded higher <α> values. The calculated <α> value at the PBE0/6-311+G(d,p) level, which was a high <α> value, differed by about 13%, 17%, 26%, 25%, and 26% from the MP2, B3LYP, CAM-B3LYP, ωB97X-D, and M06-2X values, respectively. As regards Δα, the calculated value of PDBT at the PBE0/6-311+G(d,p) level, which was a high Δα value, differed by about 20%, 30%, 40%, 35%, and 38% from the MP2, B3LYP, CAM-B3LYP, ωB97X-D, and M06-2X values, respectively. At the same level, the α values evolved in the following order: $\langle\alpha\rangle_{\text{CAM–B3LYP}} < \langle\alpha\rangle_{\text{M06–2X}} < \langle\alpha\rangle_{\text{ωB97X–D}} < \langle\alpha\rangle_{\text{B3LYP}} < \langle\alpha\rangle_{\text{MP2}} < \langle\alpha\rangle_{\text{PBE0}}$ and $\Delta\alpha_{\text{CAM–B3LYP}} < \Delta\alpha_{\text{M06–2X}} < \Delta\alpha_{\text{ωB97X–D}} < \Delta\alpha_{\text{B3LYP}} < \Delta\alpha_{\text{MP2}} < \Delta\alpha_{\text{PBE0}}$.

The donor-acceptor strength plays a major role in controlling the NLO of compounds. In our studied piperazine, and due to the intermolecular hydrogen bonding formed between the hydrogen of the protonated nitrogen atom of piperazine and the negatively charged oxygen of the picrate anion, the donor-acceptor strength was considerably higher in PDBT. The same finding was reported by Ambika *et al.* [62] and Hegde *et al.* [63] in their studies of the NLO properties of piperazine-1,4-diium bis(2,4-dichlorobenzoate) and piperazine-1,4-diium tetrachloridocuprate(II) dihydrate, respectively. According to the results presented in Table 4 and Fig. 4, there was a significant difference between the β_{tot}, $\beta_{//}$, and β_{HRS} values calculated using the B3LYP, PBE0, CAM-B3LYP, and M06-2X functionals. The β_{HRS} value obtained using the B3LYP functional (73245.21 a.u.) was substantially higher than those obtained using the MP2, PBE0, CAM-B3LYP, ωB97X-D, and M06-2X levels (Fig. 4). The average $\langle\beta_{HRS}\rangle$ on the equiprobable orientations was taken by a molecule, and the piperazine was placed in the *xy*-plane (Fig. 5). The calculations also showed that β made the most contribution along the *x*-axis because the *x*-axis was the major CT axis in the studied piperazine.

Regarding β_{tot}, the B3LYP level showed a somewhat greater propensity to deliver results divergent from the other levels. A significant difference was observed between the $\beta_{//}$ values obtained using the M06-2X compared to B3LYP, PBE0, CAM-B3LYP, and ωB97X-D functionals. The calculated β_{HRS} value of the studied piperazine at the B3LYP/6-311+G(d,p) level, which delivered a high β_{HRS} value, differed by about 25%, 18%, 26%, 37%, and 36% from the values obtained by the MP2, PBE0, CAM-B3LYP, ωB97X-D, and M06-2X methods, respectively. The MP2 method yielded a value that was closer to the CAM-B3LYP

Table 4. Mean Polarizability <α>, Anisotropy Polarizability Δα, Gas-Phase EFISHG $\beta_{//}$, the HRS First Hyperpolarizability β_{HRS}, and Depolarization Ratios (DR) Obtained at 1064 nm Using Five DFT Functionals and MP2 at the 6-311+G(d,p) Basis Set

	<α>	Δα	$\beta_{//}$	β_{tot}	β_{HRS} (DR)
B3LYP	216.32	261.32	20766.21	171093.50	73245.21 (3.02)
PBE0	261.25	371.65	22562.25	106136.56	59610.65 (2.59)
CAM–B3LYP	193.26	223.65	27369.30	138535.69	53605.21 (2.65)
ωB97X–D	197.56	241.32	39640.32	125651.25	45598.56 (2.44)
M06–2X	194.65	230.69	42211.25	120156.28	46353.26 (2.39)
MP2	232.50	294.54	26211.02	141451.56	54715.56 (2.65)

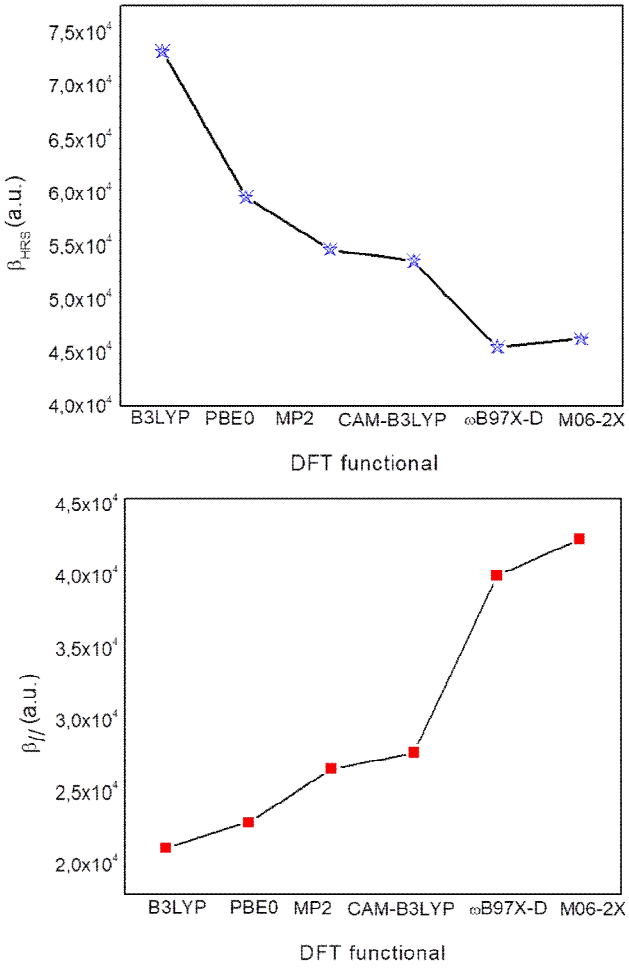

Fig. 4. The β_{HRS} (left) and $\beta_{//}$ (right) of PDBT determined at different levels of approximation.

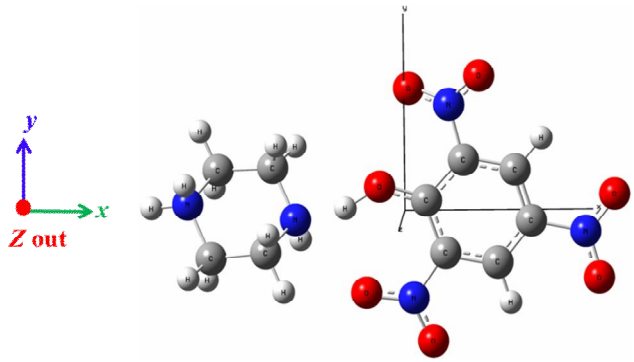

Fig. 5. The orientation of the studied PDBT during calculations.

functional than the B3LYP, PBE0, ωB97X-D, and M06-2X. The calculated β_{HRS} value differed by about 2% from that obtained by the CAM-B3LYP. Concerning β_{tot}, the calculated $\beta_{//}$ value at the same B3LYP/6-311+G(d,p) level differed by about 17%, 38%, 19%, 26%, and 29% from those obtained at the MP2, PBE0, CAM-B3LYP, ωB97X-D, and M06-2X levels, respectively. The high M06-2X $\beta_{//}$ value differed by about 26%, 50%, 46%, 35%, and 6% from the MP2, B3LYP, PBE0, CAM-B3LYP, and ωB97X-D levels, respectively. The evolution of the scattering intensity with respect to the Ψ of incident light was also investigated in this study. The scattering intensity corresponding to the Ψ varied from -180° to 180° with a step-size of 1°. Figure 6 shows the calculated scattering intensities at the B3LYP, PBE0, CAM-B3LYP, ωB97X-D, and M06-2X functionals, presented with lobes in black, green, blue, red, and orange,

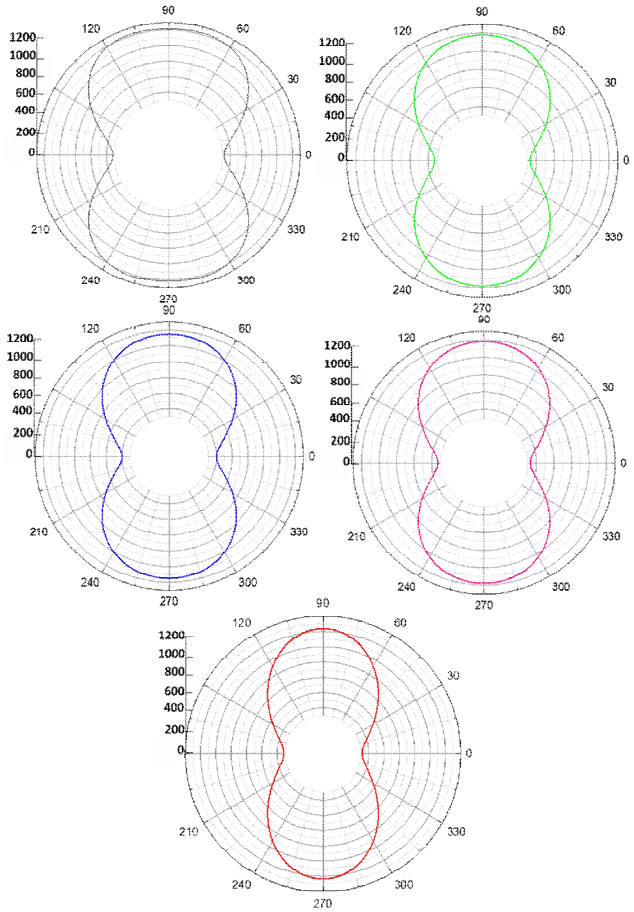

Fig. 6. HRS intensity as a function of the angle of polarization at 694.56 nm obtained with five DFT levels, including B3LYP, PBE0, CAM-B3LYP, ωB97X-D, and M06-2X, and presented in black, green, blue, red, and orange, respectively, at the same 6-311+G(d,p) basis set.

respectively. The results showed that the calculated HRS intensities presented by lobes were not exact and strongly affected by the calculation level. The results showed complete discrimination between the highest values obtained using the B3LYP and those values obtained by other DFT functionals. Theoretical studies show that an increase in the degree of correlation or the basis set size can lead to results closer to the experimental data [64]. They showed that the differences between the calculated shape and measured scattered intensity were also related to the overestimation of the octupolar contribution of β by theoretical calculations. The scattering intensity corresponding to the Ψ of the framework of 1,3-thiazolium-5-thiolates mesoionic compounds was studied by Lu *et al.* [65]. They demonstrated that the scattering intensity enhanced significantly and dipolar characteristics slightly increased for each molecule at the fundamental wavelength of 1180 nm. They confirmed that the HRS intensity gradually increased at any Ψ, which is in agreement with what was observed in the present study. All the five functionals, including DFT B3LYP, PBE0, CAM-B3LYP, ωB97X-D, and M06-2X, revealed that β_{HRS} and $\beta_{//}$ were inversely correlated (Table 4 and Fig. 4); that is, high β_{HRS} values were obtained for low $\beta_{//}$ values.

Frontier Molecular Orbitals (FMOs)

In this section, HOMO and LUMO isosurfaces (Fig. 8), their energies, and their energy gap ($\Delta\varepsilon$) are presented and analysed (Table 5).

The results showed that the $\Delta\varepsilon$ varied from 1.05 to 4.47 eV using the B3LYP and ωB97X-D functionals, respectively (Table 5 and Fig. 7). The decrease in the $\Delta\varepsilon$ values explains the eventual CT interaction taking place within PDBT [66-67], where the donor-acceptor strength is considerably high due to the intermolecular hydrogen bonding [24]. Compared to other DFT levels used in this study, the B3LYP/6-311+G(d,p) level yielded a low $\Delta\varepsilon$ value (1.05 eV). The PBE0 functional resulted in a value (2.23 eV) close to the experimental one (2.63 eV) [24]

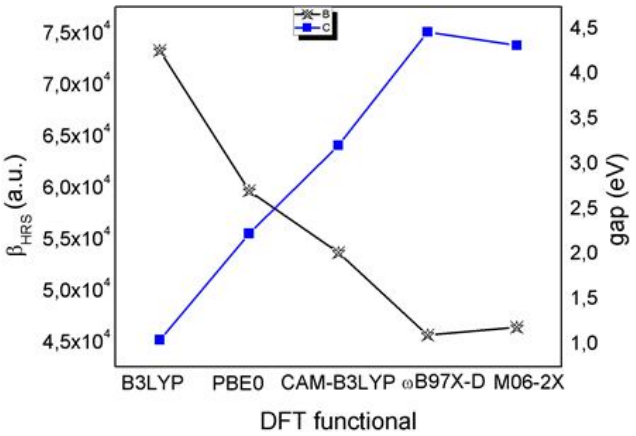

Fig. 7. β_{HRS} (a.u.) and $\Delta\varepsilon$ (eV) of the PDBT determined at the PBE0/6-311+G(d,p) level.

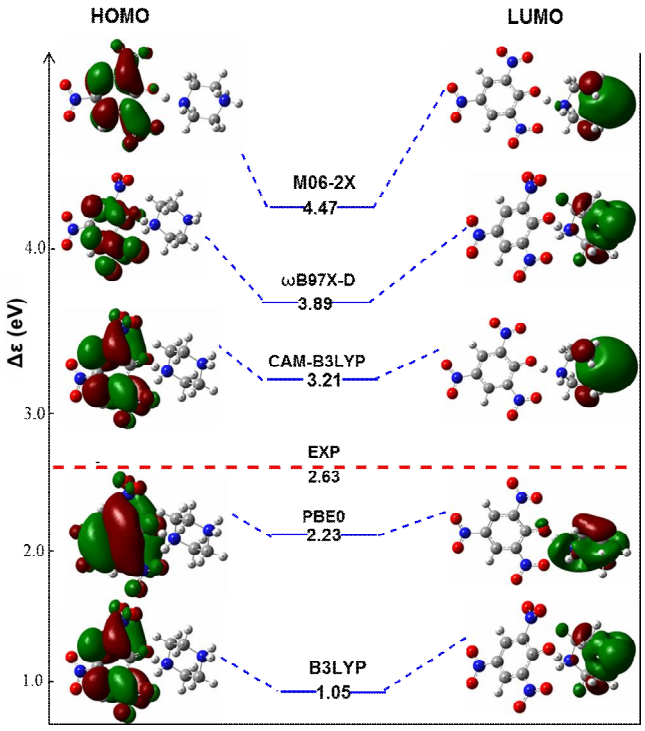

Fig. 8. HOMO and LUMO orbitals of PDBT and their Δε (eV) computed at the PBE0/6-311+G(d,p) level.

Table 5. E_{HOMO}, E_{LUMO}, Δε (eV), and the β_{HRS} (a.u.) of PDBT Obtained Using Five DFT Levels at the 6-311+G(d,p) Basis Set

	E_{HOMO}	E_{LUMO}	Δε	β_{HRS}
B3LYP	-3.23	-2.18	1.05	73245.21
PBE0	-3.56	-1.33	2.23	59610.65
CAM-B3LYP	-5.31	-2.1	3.21	53605.21
ωB97X-D	-5.46	-0.99	4.47	45598.56
M06-2X	-4.58	-0.26	4.32	46353.26
Exp[a]			2.63	

Note: [a] = experimental Δε [24].

obtained using a Tauc plot [68-69]. A combined theoretical and experimental study of 2-thioxo-3-N,(4-methylphenyl) thiazolidine-4 one supported the suitability of the PBE0 level to predict the Δε [70].

The analysis of the frontier molecular orbital isosurfaces showed that whereas the HOMOs were delocalized in the picrate anion using the five DFT levels (Fig. 8), the LUMOs were centred in piperazine cations. The picrate acted as an electron donor while the piperazine acted as an electron acceptor. The donor-withdrawing strength was considerably high due to the presence of strong hydrogen bonds, which was in line with what Ghosh *et al.* [71] observed in their study of a pair of hydrogen bond donor-acceptor of 1,2,4,5-tetracyanobenzene. Higher values of PDBT were caused by the decrease in the Δε (Table 5 and Fig. 7); *i.e.*, high $\boldsymbol{\beta_{HRS}}$ values were obtained for low Δε values.

Global Chemical Reactivity Descriptors

The GCRD were estimated using HOMO and LUMO energies to better understand the chemical reactivity of PDBT. Koopmans' theorem [72-73] was used to calculate the chemical reactivity of molecular systems. The following equations were used to calculate the previously mentioned descriptors:

$$\chi = \left(\frac{IP + EA}{2}\right), \eta = \left(\frac{IP - EA}{2}\right), \omega = \frac{\mu^2}{2\eta} \quad (10)$$

where IP = E_{HOMO} and EA = E_{LUMO} represent the ionization potential and electron affinity, respectively. B3LYP, PBE0, CAM-B3LYP, ωB97X-D, and M06-2X functionals with the 6-311+G(d,p) basis set were used to evaluate the GCRD (χ, η, S, and ω). Table 6 presents the calculated values. The calculated IP and EA of PDBT by B3LYP, PBE0, CAM-

Table 6. Calculated Values of the GCRD for PDBT Using the B3LYP, PBE0, CAM-B3LYP, ωB97X-D, and M06-2X Functional at the Same 6-311+G(d,p) Basis Set

	IP	EA	χ	η	S	ω
B3LYP	3.23	2.18	2.70	0.53	0.95	6.97
PBE0	3.56	1.33	2.44	1.11	0.45	2.68
CAM–B3LYP	5.31	2.10	3.71	1.61	0.31	4.28
ωB97X–D	5.46	0.99	3.23	2.23	0.22	2.33
M06–2X	4.58	0.26	2.42	2.16	0.23	1.36

B3LYP, ωB97X-D, and M06-2X functionals were 3.23, 3.56, 5.31, 5.46, and 4.58 (eV) and 2.18, 1.33, 2.10, 0.99, and 0.26 (eV), respectively. It is worth mentioning that η, which is an important factor in measuring molecular stability and reactivity, indicates that CT takes place within a molecule. The obtained η values at the B3LYP, PBE0, CAM-B3LYP, ωB97X-D, and M06-2X functionals were 0.53, 1.11, 1.61, 2.23, and 2.16 (eV), respectively. According to the results of the GCRD, a high η value (2.23; eV) was obtained at the ωB97X-D level, suggesting a low intramolecular CT.

Molecular Electrostatic Potential Analysis

As shown in Fig. 9, the three-dimensional MESP of PDBT was calculated from the optimized molecular structure using the B3LYP/6-311+G(d,p) level. It is worth noting that the PDBT potential increased in the following order: red, orange, yellow, green, and blue. The blue colour represents the areas with the highest positive electrostatic potential, which denotes the strongest attraction. However, the red colour represents the areas with the most negative electrostatic potential, which reflects the strongest repulsion. The negative (red, orange, and yellow) areas of the MESP were related to the electrophilic reactivity. Furthermore, the red colour of the two-dimensional MESP indicates that the region near oxygen was rich in electrons. The hydrogen atoms (blue region) in the compound under consideration reacted with nucleophilic sites.

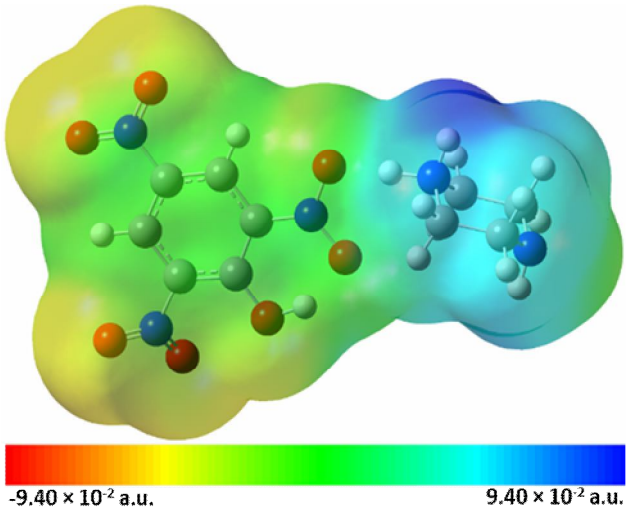

Fig. 9. The three-dimensional MESP for PDBT obtained at the B3LYP/6-311+G(d,p) level.

CONCLUSIONS

The current study investigated the structural, vibrational, linear, and NLO properties of PDBT using theoretical calculations based on the DFT method at several functionals. The IR spectral analysis and complete vibrational assignments were presented. These assignments are important to understand the molecular structure. Key results included the following: 1) Predicted geometrical parameters showed a very good correlation with their corresponding experimental ones; 2) Vibrational frequency shifts clearly indicated the presence of non-covalent interactions; also, a good correlation was observed between the calculated and experimental vibration frequencies; 3) An inverse relationship was observed between $\Delta\varepsilon$ and β; 4) The NLO results predicted at different DFT levels confirmed the NLO activity of PDBT; 5) The results obtained from the five DFT levels revealed that β_{HRS} and $\beta_{//}$ were inversely correlated; 6) Sometimes, the choice of the DFT functional had a noticeable effect on the linear and NLO calculated values of the studied piperazine; 7) According to the MESP map, the negative potential sites were on the electronegative atoms while the positive potential sites were around the hydrogen atoms. The high hardness value suggests a low intramolecular CT. This study not only helps researchers understand the NLO properties of piperazine-based molecules but also provides rich insight into designing and developing materials with excellent NLO properties.

ACKNOWLEDGEMENTS

The authors would like to acknowledge the help and support of the Algerian Ministry of Higher Education and Scientific Research as well as the General Directorate of Scientific Research and Technological Development.

REFERENCES

[1] Zhao, Y.; Yang, Y.; Sun, H. B., Nonlinear meta-optics towards applications, *PhotoniX*, **2021**, *2*, 3, DOI: 10.1186/s43074-021-00025-1.

[2] Klimmer, S.; Ghaebi, O.; Gan, Z.; George, A.; Turchanin, A.; Cerullo, G.; Soavi, G., All-optical polarization and amplitude modulation of second-harmonic generation in atomically thin semiconductors, *Nat. Photon*. **2021**, *15*, 837-842, DOI: 10.1038/s41566-021-00859-y.

[3] Semin, S.; Li, X.; Duan, Y.; Rasing, T., Nonlinear optical properties and applications of fluorenone molecular materials, *Adv. Opt. Mater.* **2021**, *9*, 2100327, DOI: 10.1002/adom.202100327.

[4] Karnan, C.; Rhoda, J. C.; Manikandan, A.; Vinitha, G., Supramolecular assembly of morpholin-4-ium hydroxy(diphenyl)acetate-structural, spectral and nonlinear optical analyses, *J. Mol. Struct.* **2022**, *1250*, 131719, DOI: 10.1016/j.molstruc.2021.131719.

[5] Mahalakshmi, P.; Balraj, V.; Murugasen, P.; Vinitha, G.; Ragavendrane, V., Synthesis, structural-spectral characterization and density functional theoretical studies of pyridine-4-carbohydrazide bis(4-hydroxynitrobenzene), *J. Mol. Struct.* **2022**, *1247*, 131362, DOI: 10.1016/j.molstruc.2021.131362.

[6] Biaggio, I., Organic materials are more suitable due to their high electronic susceptibility, *Chem. Eur. J.* **2022**, *28*, 202103168, DOI: 10.2002/chem.202103168.

[7] Álvarez, D.; Menéndez, I.; López, M. R., Computational design of rhenium(I) carbonyl complexes for anticancer photodynamic therapy, *Inorg. Chem.* **2022**, *61*, 439-455, DOI: 10.1021/acs.inorgchem.1c03130.

[8] Khan, I. M.; Ahmad, A.; Ullah, M. F., Synthesis, spectroscopic investigations, antimicrobial and DNA binding studies of a new charge transfer complex of o-phenylenediamine with 3,5-dinitrosalicylic acid, *Spectrochim. Acta A Mol. Biomol. Spectrosc*. **2013**, *102*, 82-87, DOI: 10.1016/j.saa.2012.10.027.

[9] Andrade, S. M.; Costa, S. M. B.; Pansu, R., Structural changes in W/O Triton X-100/cyclohexane-hexanol/water microemulsions probed by a fluorescent drug Piroxicam, *J. Colloid Interface Sci*. **2000**, *226*, 260-268, DOI: 10.1006/jcis.2000.6821.

[10] Eychmüller, A.; Rogach, A. L., Chemistry and photophysics of thiol-stabilized II-VI semiconductor nanocrystals, *Pure Appl. Chem.* **2000**, *72*, 179-188, DOI: 10.1351/pac200072010179.

[11] de Jong, J. J.; Lucas, L. N.; Kellogg, R. M.; Van Esch, J. H.; Feringa, B. L., Reversible optical transcription of supramolecular chirality into molecular chirality, *Science*, **2004**, *304*, 278-281, DOI: 10.1126/science.1095353.

[12] Essid, M.; Marouani, H.; Rzaigui, M., 1-Methyl-piperazine-1,4-dium bis(hydrogen oxalate), *Acta Cryst.* **2014**, *E70*, 326-327,DOI: 10.1107/S1600536814003559.

[13] Mullai, R. U.; Sivavishnu, D.; ArulJothi, R.; Vinitha, G.; Gopinath, S.; Vetrivel, S., Third order nonlinear optical properties of piperazine calcium chloride (PCC) Crystal to enhance the optical device applications, *J. Electron. Mater.* **2020**, *49*, 454-463, DOI: 10.1007/s11664-019-07689-3.

[14] Upadhayaya, R. S.; Sinha, N.; Jain, S.; Kishore, N., Optically active antifungal azoles: synthesis and antifungal activity of (2R,3S)-2-(2,4-difluorophenyl)-3-(5-{2-[4-aryl-piperazin-1-yl]-ethyl}-tetrazol-2-yl/1-yl)-1-[1,2,4]-triazol-1-yl-butan-2-ol, *Bioorg. Med. Chem.* **2004**, *12*, 2225-2238, DOI: 10.1016/j.bmc.2004.02.014.

[15] Chaudhary, P.; Kumar, R.; Verma, A. K.; Singh, D.; Yadav, V.; Chhillar, A. K.; Sharma, G. L.; Chandra, R., Synthesis and antimicrobial activity of N-alkyl and N-aryl piperazine derivatives, *Bioorg. Med. Chem.***2006**, *14*, 1819-1826, DOI: 10.1016/j.bmc.2005.10.032.

[16] Kharb, R.; Bansal, K.; Sharma, A. K., A valuable insight into recent advances on antimicrobial activity of piperazine derivatives, *Der. Pharma. Chem.* **2012**, *4*, 2470-2488.

[17] Maurya, R. C.; Sharma, P.; Roy, S., Synthesis and characterization of some mixed-ligand picrate complexes of nickel(II) involving heterocyclic nitrogen donors, *Synth. React. Inorg. Met. Org. Chem.* **2003**, *33*, 683-698, DOI: 10.1081/SIM-120020332.

[18] Dhanabal, T.; Sethuram, M.; Amirthaganesan, G.; Das, S. K., Spectral, thermal, structural, optical and antimicrobial activity studies on 2-methylimidazolinium picrate-an organic charge transfer complex, *J. Mol. Struct.* **2013**, *1045*, 112-123, DOI: 10.1016/j.molstruc.2013.03.043.

[19] Wang, Z. L.; Jia, L. H., Three-dimensional network in piperazine-1,4-diium-picrate-piperazine (1/2/1), *Acta Cryst. E*. **2008**, *64*, 665-666,

DOI: 10.1107/S1600536808005710.

[20] Kavitha, C. N.; Jasinski, J. P.; Anderson, B. J.; Yathirajan, H. S.; Kaur, M., 1-[4-(4-Hydroxyphenyl)piperazin-1-yl]ethanone, *Acta Cryst. E*. **2013**, *69*, 1671-1671, DOI: 10.1107/S1600536813028031.

[21] Loughlin, W. A.; McCleary, M. A.; Healy, P. C., Conformational isomerism in 3-(Z)-isobutylidene-1-acetylpiperazine-2,5-dione, *Acta Crystallogr. Sect. E* **2003**, *59*, 1807-1809, DOI: 10.1107/S16005368030237.

[22] Song, Y.; Kumar, C.; Nethravathi, G. B.; Naveen, S.; Li, H., Cinnarizinium picrate, *Acta Cryst. E* **2012**, *68*, 1747-1747, DOI: 10.1107/S1600536812020764.

[23] Kavitha, C. N.; Kaur, M.; Anderson, B. J.; Jasinski, J. P.; Yathirajan, H. S., 1-Piperonylpiperazinium picrate, *Acta Cryst. E* **2014**, *70*, 208-209, DOI: 10.1107/S1600536814001524.

[24] Suguna, S.; Anbuselvi, D.; Jayaraman, D.; Nagaraja, K. S.; Jeyaraj, B., Synthesis, growth, structural and optical studies of organic nonlinear optical material-Piperazine-1,4-diium bis-2,4,6-trinitrophenolate, *Spectrochim. Acta A*. **2014**, *32*, 330-338, DOI: 10.1016/j.saa.2014.04.095.

[25] Stephens, P. J.; Devlin, F. J.; Chabalowski, C. F.; Frisch, M. J., *Ab initio* calculation of vibrational absorption and circular dichroism spectra using density functional force fields, *J. Phys. Chem*. **1994**, *98*, 11623-11627, DOI: 10.1021/j100096a001.

[26] Binning, R. C.; Curtiss, L. A., Compact contracted basis sets for third-row atoms: Ga-Kr, *J. Comput. Chem.* **1990**, *11*, 1206-1216, DOI: 10.1002/jcc.540111013.

[27] Krishnan, R.; Binkley, J. S.; Seeger, R.; Pople J. A., Self-consistent molecular orbital methods. XX. A basis set for correlated wave functions, *J. Chem. Phys.* **1980**, *72*, 650, DOI: 10.1063/1.438955.

[28] McLean, A. D.; Chandler, G. S., Contracted Gaussian basis sets for molecular calculations. I. Second row atoms, Z = 11-18, *J. Chem. Phys.* **1980**, *72*, 5639, DOI: 10.1063/1.438980.

[29] Jamroz, M. H., Vibrational Energy Distribition Analysis (VEDA 4) Program, Warsaw, Poland, **2004**.

[30] Møller, C., Plesset, M. S., Note on an approximation treatment for many-electron systems, *Phys. Rev.* **1934**, *46*, 618-622, DOI: 10.1103/PhysRev.46.618.

[31] Adamo, C.; Barone, V., Toward reliable density functional methods without adjustable parameters: The PBE0 model, *J. Chem. Phys.* **1999**, *110*, 6158, DOI: 10.1063/1.478522.

[32] Yanai, T.; Tew D. P.; Handy, N. C., A new hybrid exchange-correlation functional using the Coulomb-attenuating method (CAM-B3LYP), *Chem. Phys. Lett.* **2004**, *393*, 51-57, DOI: 10.1016/j.cplett.2004.06.011.

[33] Chai, D. J.; Head-Gordon, M., Systematic optimization of long-range corrected hybrid density functionals, *J. Chem. Phys.* **2008**, *128*, 084106, DOI: 10.1063/1.2834918.

[34] Zhao, Y.; Truhlar, D. G., Density functional for spectroscopy: No long-range self-interaction error, good performance for Rydberg and charge-transfer states, and better performance on average than B3LYP for ground states, *J. Phys. Chem. A*, **2006**, *110*, 13126-13130, DOI: 10.1021/jp066479k.

[35] Frisch, M. J., *et al.* Gaussian 09, Gaussian, Inc., Wallingford CT, **2009**.

[36] Dennington, R.; Keith, T.; Millam, J. M., GaussView version 5, SemichemInc., Shawnee Mission, KS, **2009**.

[37] Lu, T.; Chen, F., Multiwfn: A multifunctional wavefunction analyzer, *J. Comput. Chem*. **2012**, *33*, 580-592, DOI: 10.1002/jcc.22885.

[38] Lu, T., Multiwfn, version 3.7(dev). http://sobereva.com/multiwfn/ (accessed Sep. 9, 2019).

[39] Bersohn, R.; Pao, Y. H.; Frisch, H. L., Double quantum light scattering by molecules, *J. Chem. Phys.* **1966**, *45*, 3184, DOI: 10.1063/1.1728092.

[40] Zandler, M. E.; D'Souza, F., The remarkable ability of B3LYP/3-21G(*) calculations to describe geometry, spectral and electrochemical properties of molecular and supramolecular porphyrin-fullerene conjugates, *C. R. Chim.* **2006**, *9*, 960-981, DOI: 10.1016/j.crci.2005.12.008.

[41] Orio, M.; Pantazis, D. A.; Neese, F., Density functional theory, *Photosynth Res.* **2009**, *102*, 443-453, DOI: 10.1007/s11120-009-9404-8.

[42] Wan, R.; Yin, L. H.; Han, F.; Wang, B.; Wang, J. T., 2-(2,4-Dichlorophenyl)-3-[5-(4-methoxyphenyl)-1,3,4-thiadiazol-2-yl]-1,3-thiazolidin-4-one, *Acta Cryst. E.* **2008**, *1*, 795, DOI: 10.1107/S1600536808008465.

[43] Pulay, P.; Fogarasi, G.; Pongor, G.; Boggs, J. E.; Vargha, A., Combination of theoretical *ab initio* and experimental information to obtain reliable harmonic force constants. Scaled quantum mechanical (QM) force fields for glyoxal, acrolein, butadiene, formaldehyde, and ethylene, *J. Am. Chem. Soc.* **1983**, *105*, 7037-7047, DOI: 10.1021/ja00362a005.

[44] Alecu, I. M.; Zheng, J.; Zhao, Y.; Truhlar, D. G., Computational thermochemistry: Scale factor databases and scale factors for vibrational requencies obtained from electronic model chemistries, *J. Chem. Theory. Comput.* **2010**, *6*, 2872-2887, DOI: 10.1021/ct100326h.

[45] Bardakcı, T.; Kumru, M.; Guner, S., Molecular structure, vibrational and EPR spectra of Cu(II) chloride complex of 4-amino-1-methylbenzene combined with quantum chemical calculations, *J. Mol. Struct.* **2013**, *1054*, 76-82, DOI: 10.1016/ j.molstruc.2013.09.025.

[46] Bernardino, A. C. S. S.; Teixeira, A. M. R.; de Menezes, J. E. S. A.; Pinto, C. C. C.; Santos, H. S; Freire, P. T. C.; Coutinho, H. D. M.; Junior, D. M. S.; Bandeira, P. N.; Braz-Filho, R., Spectroscopic and microbiological characterization of labdane diterpene 15,16-epoxy-4-hydroxy-labda-13(16),14-dien-3,12-dione isolated from the stems of Croton jacobinensis, *J. Mol. Struct.* **2017**, *1147*, 335-344, DOI: 10.1016/ j.molstruc.2017.06.084.

[47] Tamer, O.; Avcı, D.; Atalay, Y., The effects of electronegative substituent atoms on structural, vibrational, electronic and NLO properties of some 4-nitrostilbene derivates, *Spectrochim. Acta A* **2015**, *136*, 644-650, DOI: 10.1016/j.saa.2014.09.078.

[48] Rafilovich, M.; Bernstein, J., Serendipity and four polymorphic structures of benzidine, $C_{12}H_{12}N_2$, *J. Am. Chem. Soc.* **2006**, *128*, 12185-12191,DOI: 10.1021/ ja063224b.

[49] Chain, F.; Romano, E.; Leyton, P.; Paipa, C.; Catalan, C. A. N.; Fortuna, M. A.; Brandan, S. A., An experimental study of the structural and vibrational properties of sesquiterpene lactone cnicin using FT-IR, FTRaman, UV-Vis and NMR spectroscopies, *J. Mol. Struct.* **2014**, *1065*, 160-169, DOI: 10.1016/ j.molstruc.2014.02.057.

[50] Gunasekaran, S.; Anita, B., Spectral investigation and normal coordinate analysis of piperazine, *Indian J. Pure Appl. Phys.* **2008**, *46*, 833-838.

[51] Balakina, M. Y.; Nefediev, S. E., The choice of basis set for calculations of linear and nonlinear optical properties of conjugated organic molecules in gas and in dielectric medium by the example of p-nitroaniline, *Comput. Mater. Sci.* **2007**, *38*, 467-472, DOI: 10.1016/j.commatsci.2005.05.011.

[52] Avci, D.; Bas, A.; Lu, O.; Atalay, Y., Effects of different basis sets and donor-acceptor groups on linear and second-order nonlinear optical properties and molecular frontier orbital energies, *Int. J. Quantum Chem*. **2011**, *111*, 130-147, HYPERLINK "https://doi.org/10.1002/qua.22416" DOI: 10.1002/qua.22416 .

[53] Roy, R. S.; Nandi, P. K., Exploring bridging effect on first hyperpolarizability, HYPERLINK "https://doi.org/10.1039/2046-2069/2011" \o "Link to journal home page" *RSC Adv.* **2015**, *5*, 103729-103738, HYPERLINK "https://doi.org/10.1039/ C5RA22615E"\o "Link to landing page *via* DOI" DOI: 10.1039/C5RA22615E .

[54] Hatua, K.; Nandi, P. K., HYPERLINK "https://scholar.google.com/citations?view_op=view_citation&hl=ja&user=XOpVzMgAAAAJ&citation_for_view=XOpVzMgAAAAJ:ufrVoPGSRksC" Beryllium–cyclobutadiene multidecker inverse sandwiches: electronic structure and second-hyperpolarizability, *J. Phys. Chem. A.* **2013**, *117*, 12581-12589, HYPERLINK "https://doi.org/10.1021/jp407563f" \o "DOI URL" DOI: 10.1021/jp407563f.

[55] Hatua, K.; Nandi, P. K., Double coned inverse sandwich complexes [M-(η4-C4H4)-M′] of Gr-IA and Gr-IIA metals: Theoretical study of electronic of structure and second hyperpolarizability, *J. Mol. Model*. **2014**, *20*, 2440-2449, HYPERLINK "https://doi.org/10.1021/j100025a017" \o "DOI URL" DOI: 10.1021/j100025a017.

[56] Adamo, C.; Cossi, M.; Scalmani, G., HYPERLINK "https://www.sciencedirect.com/science/article/abs/pii/ S0009261499005151"\l "!" Barone , V. Accurate static polarizabilities by density functional theory: Assessment of the PBE0 model, *Chem. Phys. Lett.* **1999**, *307*, 265-271, HYPERLINK

"https://doi.org/10.1016/S0009-2614(99)00515-1" \t "_blank" \o "Persistent link using digital object identifier" DOI: 10.1016/S0009-2614(99)00515-1.

[57] Sabirov, D. S., Polarizability of C_{60} fullerene dimer and oligomers: The unexpected enhancement and its use for rational design of fullerene-based nanostructures with adjustable properties, *RSC Adv.* **2013**, *3*, 19430-19439, DOI: 10.1039/C3RA42498G.

[58] Hadji, D.; Rahmouni, A.; Hammoutène, D.; Zekri, O., First theoretical study of linear and nonlinear optical properties of diphenyl ferrocenyl butene derivatives, *J. Mol. Liq.* **2019**, *286*, 110939, DOI: 10.1016/j.molliq.2019.110939.

[59] Ye, J. T.; Liu, J. H.; Zhang, Q., Tuning of second-order nonlinear optical properties based on [2.2]paracyclophanes isomer: The relative configuration and polarizable environment, *J. Phys. Chem. C.* **2020**, *124*, 21692-21701, DOI: 10.1021/acs.jpcc.0c05980.

[60] Hadji, D.; Haddad, B.; Brandán, S. A.; Panja, S. K.; Paolonee, A.; Drai, M.; Villemin, D.; Bresson, S.; Rahmouni, M., Synthesis, NMR, Raman, thermal and nonlinear optical properties of dicationic ionic liquids from experimental and theoretical studies, *J. Mol. Struct.* **2020**, *1220*, 128713, DOI: 10.1016/j.molstruc.2020.128713.

[61] Ye, J.; Liu, J.; Zhang, Q.; Qiu, Y.; Wang, L. H., Tuning of second-order nonlinear optical properties tuning of second-order nonlinear optical properties based on [2.2]paracyclophanes Isomer: the based on [2.2]paracyclophanes isomer: Relative configuration and polarizable environment, *J. Phys. Chem. C.* **2020**, *124*, 21692-21701, DOI: 10.1021/acs.jpcc.0c05980.

[62] Ambika, V. R.; Jayalakshmi, D.; Narendran, K.; Athimoolam, S.; Valan, M. F.; Kamalarajan, P., Growth, structural, spectral, optical and thermal studies of a novel third-order nonlinear optical single crystal: Piperazine-1,4-diium bis(2,4-dichlorobenzoate), *J. Mol. Struct.* **2015**, *139*, 302-306, DOI: 10.1016/j.saa.2014.12.069.

[63] Hegde, T. A.; Dutta, A.; Girisun, T. C. S.; Vinitha, G., A novel organic-inorganic ionic cocrystal-piperazine-1,4-diium tetrachloridocuprate(II) dihydrate delivering efficient optical limiting, *Chem. Phys. Lett.* **2021**, *781*, 138971, DOI: 10.1016/j.cplett.2021.138971.

[64] Castet, F.; Bogdan, E.; Plaquet, A.; Ducasse, L.; Champagne, B.; Rodriguez, V., Reference molecules for nonlinear optics: A joint experimental and theoretical investigation, *J. Chem. Phys.* **2012**, *136*, 024506, DOI: 10.1063/1.3675848.

[65] Liu, Z.; Tian, Z.; Lu, T.; Hua, S., Theoretical framework of 1,3-thiazolium-5-thiolates mesoionic compounds: Exploring the nature of photophysical property and molecular nonlinearity, *J. Phys. Chem. A.***2020**, *124*, 5563-5569, DOI: 10.1021/acs.jpca.0c03166.

[66] Miar, M.; Shiroudi, A.; Pourshamsian, K.; Oliaey, A. R.; Hatamjafari, F., Theoretical investigations on the HOMO-LUMO gap and global reactivity descriptor studies, natural bond orbital, and nucleus-independent chemical shifts analyses of 3-phenylbenzo[d]thiazole-2(3H)-imine and its *para*-substituted derivatives: Solvent and substituent effects, *J. Chem. Res.* **2019**, *45*, 147-158, DOI: 10.1177/1747519820932091.

[67] Marzi, M.; Shiroudi, A.; Pourshamsian, K.; Oliaey, A. R.; Hatamjafari, F., A theoretical study of the tautomerism kinetics of 4-amino-6-methyl-3-thioxo-3,4-dihydro-1,2,4- triazin-5(2H)-one in the gas phase: NBO population and NICS analysis, *J. Sulfur Chem.* **2019**, *40*, 166-184, DOI: 10.1080/17415993.2018.1548621.

[68] Dolgonos, A.; Mason, T. O.; Poeppelmeier, K. R., Direct optical band gap measurement in polycrystalline semiconductors: a critical look at the Tauc method, *J. Solid. State Chem.* **2016**, *240*, 43, DOI: 10.1016/j.jssc.2016.05.010.

[69] Viezbicke, B. D.; Patel, S.; Davis, B. E.; Birnie III, D. P., Evaluation of the Tauc method for optical absorption edge determination: ZnO thin films as a model system, *Phys. Status Solidi.* **2015**, *252*, 1700, DOI: 10.1002/pssb.201552007.

[70] Baroudi, B.; Argoub, K.; Hadji, D.; Benkouider, A. M.; Toubal, K.; Yahiaoui, A.; Djafri, A., Synthesis and DFT calculations of linear and nonlinear optical responses of novel 2-thioxo-3-N,(4-methylphenyl) thiazolidine-4 one, *J. Sulfur Chem.* **2020**, *41*, 1-16, DOI: 10.1080/17415993.2020.1736073.

[71] Ghosh, S.; Chopra, P.; Wategaonkar, S., C-H···S

Interaction exhibits all the characteristics of conventional hydrogen bonds, *Phys. Chem. Chem. Phys.* **2020**, *22*, 17482-17493, DOI: 10.1039/d0cp01508c.

[72] Parr, R. G.; Szentpály, L. V.; Liu, S., Electrophilicity index, *J. Am. Chem. Soc.* **1999**, *121*, 1922-1924, DOI: 10.1021/ja983494x.

[73] Padmanabhan, J.; Parthasarathi, R.; Subramanian, V.; Chattaraj, P., Electrophilicity-based charge transfer descriptor, *J. Phys. Chem*. **2007**, *111*, 1358-1361, DOI: 10.1021/jp0649549.